Effect of pH variation and annealing on covalently assembled nanodiamond films

Tithi Desai[a,‡] ,Naim H. Patoary[a,b,‡], Arden L. Moore[a], Adarsh D. Radadia [a,b]

[a] Institute for Micromanufacturing, Louisiana Tech University, Ruston, Louisiana, USA.

[b] Center for Biomedical Engineering and Rehabilitation Science, Louisiana Tech University, Ruston, Louisiana, USA.

[‡] indicates equal contribution as first authors

Keywords: nanodiamond, diamond thin films, nano-assembly, self-assembly; thin film assembly

ABSTRACT

This work examines the effect of using low-ionic strength zwitterionic buffer and post-deposition thermal annealing on the microstructure and thermal conductivity of continuous nanocrystalline diamond films that are deposited via the directed covalent assembly of detonation nanodiamonds. Variation of the zwitterionic buffer pH was found to tune the surface coverage, film thickness, thermal conductivity, and film morphology as quantified by apparent porosity and pore size distribution. The sequential annealing of these films up to 400 °C, showed the anticipated severance of amide bonds holding the nanodiamonds together, followed by the detrimental aggregation of the nanodiamonds to segregated islands, losing film continuity and increasing apparent porosity. The change in thermal conductivity with annealing was subjective to buffer pH, suggesting that the morphology changes associated with annealing may have a complex relationship with thermal conductivity. The thermal conductivity data were further analyzed using a phonon hopping model to quantify the degree of phonon movement across boundaries. Overall, the results demonstrate a way to achieving porous, low-cost nanocrystalline diamond thin films with tunable film morphology and thermal conductivity.

1. INTRODUCTION

Polycrystalline diamond thin films are ideal for applications in microelectromechanical systems to reduce wear[1-3], stiction, and thermal expansion [4], in harsh environments to prevent corrosion [5-7], or in medical implants such as the artificial heart or the bionic eye to improve biocompatibility [8-10]. These films are most commonly grown via chemical vapor deposition, which restricts the growth substrates to those that can resist melting, or reaction with process gases, and carbon dissolution above 350 °C [11, 12]. Further, the requirement of specialized growth chambers, vacuum conditions, precursor gases, and large power impede the reduction of cost and thus wide-scale adoption. In our prior work, we demonstrated polycrystalline diamond film preparation in the solution phase using carboxylated detonation nanodiamonds (ND-COOH) as shown in **Figure 1** [13]. The process requires the surface to be amine-terminated, which is usually achieved through hydroxylation and reaction with 2-aminopropyltriethoxy silane vapors. The resulting amine-terminated surface when cyclically reacted with carbodiimide-activated ND-COOH and a diamine linker (ethylene diamine in this case) led to the growth of a nanocrystalline diamond thin film. Concurrently, the unreacted ND-COOH in the solution can be regenerated and reactivated for use in the subsequent deposition cycle. The assembly process was demonstrated in the solution phase as well as via spin coating, both resulting in films of similar morphology and apparent porosity (Φ_{app} = 0.3-0.37). The thermal conductivity measured via the 3ω method ranged between 1-15 W m^{-1} K^{-1}, with a potential to achieve 20 W m^{-1} K^{-1} with the elimination of porosity or even greater values with improved interfacial transmission of thermal energy.

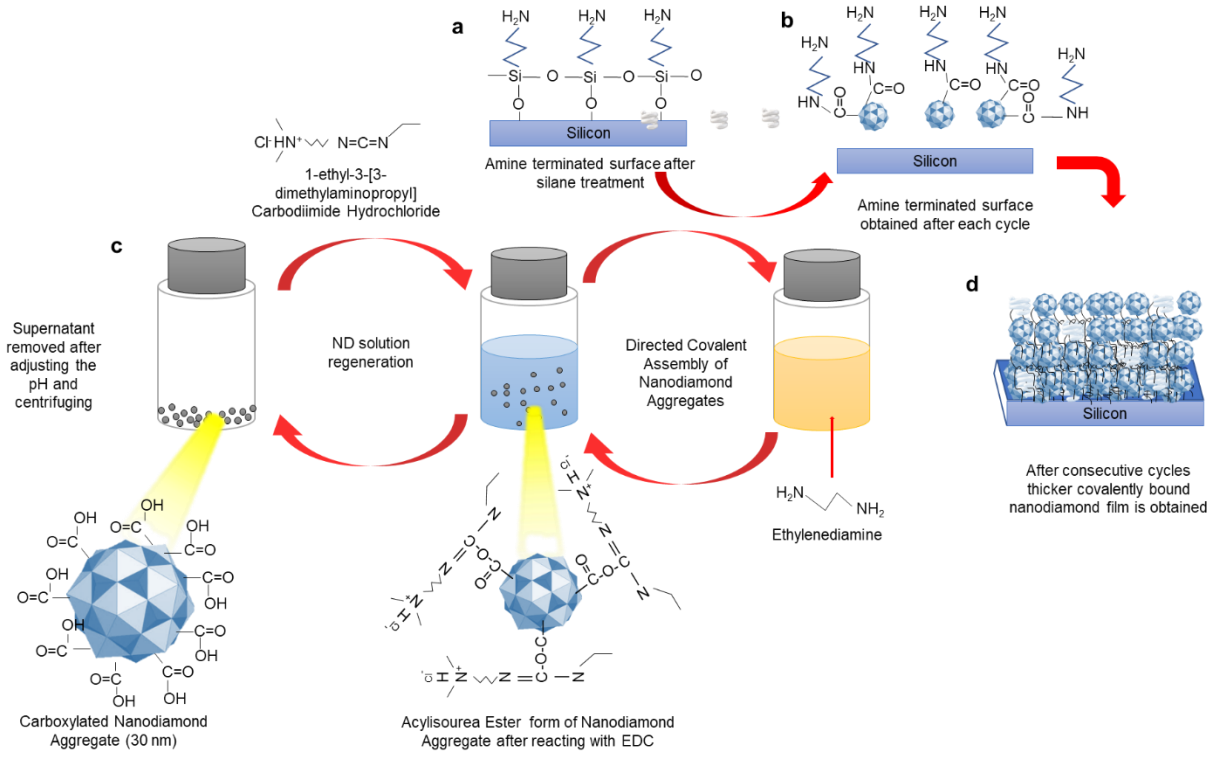

Figure 1. Process scheme for directed covalent assembly of nanodiamonds. (a) The process starts with an amine-terminated surface that was formed via the reaction of 2-aminopropyltriethoxy silane vapors with

a hydroxylated silicon dioxide surface (piranha clean, RCA-I, and RCA-II clean). (b) The amine-terminated surface was then reacted with the active acylisourea ester form of ND-COOH; this form was obtained using EDC in solution. The unreacted ester groups on the surface-tethered ND-COOH were then reacted with ethylene diamine, leaving the surface amine-terminated. (c) After each reaction cycle, the active ester form of ND-COOH in solution was hydrolyzed and regenerated by adjusting the pH, and centrifuging (RCF = 720 x g, 5 min). The ND-COOH were then suspended in fresh solution media using horn sonication (750 W, 20 kHz, 60 min). (d) Consecutive cyclic deposition of ND-COOH on the surface in this manner results in complete surface coverage, followed by an increase in film thickness.

Here, we examine the effect of the reaction medium and post-assembly annealing on the film morphology and thermal conductivity. The motivation to study thermal conduction implications of these processing variables are two-fold. First, there is a desire following our initial work to investigate if the thermal conductivity might be improved via changes in processing-induced changes in film morphology and particle-particle interfaces. Second, we seek to use thermal conductivity measurements as a means of comparing the strength of particle-particle interactions across processing variables even if the net result is a lowered thermal conductivity for a given case. Our prior work was performed using deionized water or 1 mM KCl as the reaction medium. As shown in **Figure 2**, when the carbodiimide cross-linker (EDC) is added to a horn-sonicated ND-COOH suspension in deionized water, the hydrochloride content of EDC lowers the pH and leads to particle agglomeration. This is expected to result in films with higher porosity and less mechanical integrity compared to a completely covalently bound film. Further, the size distribution of the ND-COOH in DI water changes with each regeneration, and the addition of EDC results in a different particle size distribution. Here, we chose a zwitterionic 2-ethanesulfonic acid (MES) buffer because (a) it has a strong buffering capacity in the pH range (5.5 - 8) where ND-COOH may form a stable suspension, (b) contains no free amines that interfere with the EDC cross-linker chemistry and (c) its protonation and deprotonation should not alter the ionic strength significantly. But, the use of higher ionic strength would promote particle aggregation, hence, the buffer strength was fixed at 10 mM in this study, so that the resulting ionic strength stays between 1 – 6 mM even with pH variation between 5.5 and 7. **Figure 2** shows a preliminary analysis of nanodiamond agglomerate size distribution 30 min after the addition of EDC, and after regeneration in MES buffers of pH 5.5 – 7. The MES buffers of pH 6.5 and 7 show comparatively less aggregation upon addition of EDC and after two regenerations, when compared to the MES buffers of pH 5.5 and 6. Thus we restricted our study to films assembled in the MES buffers of pH 6, 6.5, and 7.

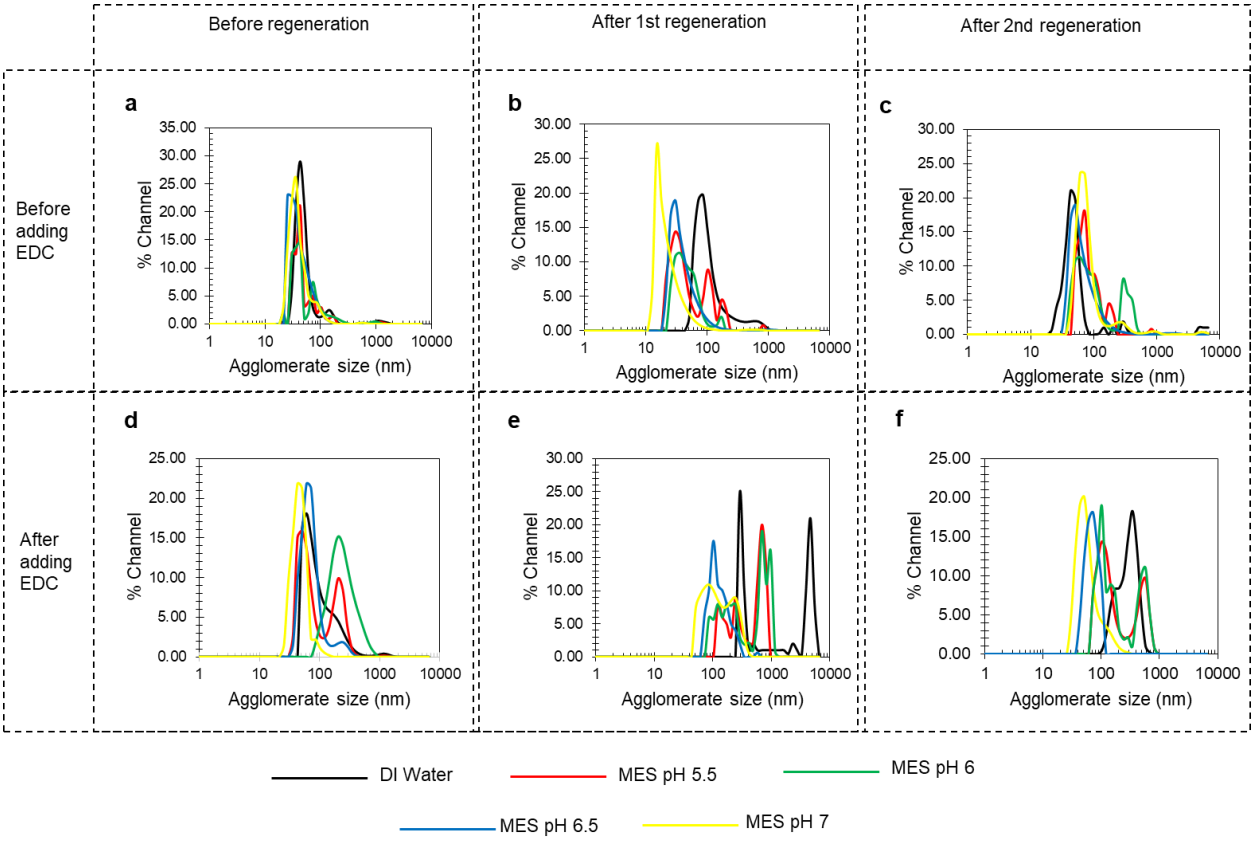

Figure 2. The shift in nanodiamond agglomerate size distribution over three consecutive assembly and regeneration cycles in MES buffer (pH 5.5, 6, 6.5, or 7) and DI water. Measurement was taken using dynamic light scattering. (a-c) Agglomerate size distribution after 1 h of horn sonication, and before activating it to an acylisourea ester form. (d-f) Agglomerate size distribution was taken 30 min after adding EDC. The % Channel indicates the intensity.

2. MATERIALS AND METHODS

2.1 Materials. Carboxylated nanodiamond aggregates (ND-COOH, 99% purity) with an average diameter of 30 nm and consisting of 3-4 nm particles were purchased from Adámas Nanotechnologies. Premium grade 1-ethyl-3-(3-dimethylaminopropyl) carbodiimide (EDC), a water-soluble carbodiimide crosslinker was used for small-length conjugation of carboxyl groups on ND-COOH to the amine group on ethylene diamine. EDC was purchased from Thermo Scientific Pierce. Ethylenediamine (EDA, 99% purity) was purchased from Alfa Aesar. Acetone (CMOS grade), 2-propanol (CMOS grade), (3-aminopropyl) triethoxysilane (99%, ACROS Organics), potassium chloride (ACS grade), ammonium hydroxide (ACS Plus), and sodium hydroxide (ACS grade) were obtained from Fisher Scientific. Solutions of 30 % hydrogen peroxide, 96 % sulfuric acid, or hydrochloric acid (ACS Plus grade) were obtained from J.T Baker Avantor. Deionized water (DI) with a minimum conductivity of 18 MΩ-cm was obtained using a Millipore deionization system.

2.2 Nanodiamond film deposition by incubation was performed on a 1.4 x 1.4 cm silicon chip. This chip size allowed us to carry out the deposition in a wide-mouth (1.6 cm) scintillation vial and perform characterizations reported here. Substrates were cleaned via Piranha, RCA-I, and RCA-II protocols followed by a DI water rinse and air drying. The surface was immediately reacted with (3-aminopropyl) triethoxysilane vapors in a vacuum desiccator for about 30 min at room temperature. The silane covered substrates were then soaked in DI water for 5 min and heated at 90 °C for 5 min to crosslink the silane layer. The amine-reactive O-acylisourea ester form of ND-COOH was prepared by horn sonicating 1 mg ND-COOH per ml of 10 mM MES buffer (pH 6, 6.5, or 7) for 1 h at room temperature, and mixing 1 mg/ml EDC. The amino-silane coated substrates were then reacted with the solution containing active ND-COOH for 30 min at room temperature. Then the substrates were rinsed in DI water for 5 min to wash off nanodiamonds (ND) not tethered covalently. Following, the substrates were dipped in EDA for 30 min, then soaked in DI water for 5 min and air-dried. The substrates were then either exposed to a solution containing an active form of either fresh or regenerated ND-COOH for the subsequent deposition cycle.

2.3 Regeneration of spent ND-COOH solution was carried out by adding 1 mM HCl in 1:500 (v/v) ratio and centrifuging at 720 rcf or 3000 rpm for 5 min. The supernatant was replaced with 10 mM MES buffer (pH 6, 6.5, or 7) and horn sonicated for 1 h before adding EDC for the next deposition cycle.

2.4 Particle size and zeta potential measurements were carried out using dynamic light scattering spectroscopy (DLS) with a laser wavelength of 780 nm on a Zetatrac (Microtrac Inc.). The average particle size distribution was averaged over 8 measurements, 30 s each. The zeta potential calculations were performed using Henry's formula for mobility to calculate the potential difference between the dispersion medium and the stationary layer of charge attached to the particle. Smoluchowski approximation was used to present results here. The use of the Huckel approximation did not change the trend seen in the zeta potential measurements. All calculation was based on properties of water at room temperature (viscosity of 0.890 cP, a dielectric constant of 79.63).

2.5 Scanning electron microscopy (SEM) was performed with a Hitachi S-4800 field-emission microscope using an accelerating voltage of 3-5kV at a magnification of 3.5k-35k to reduce artifacts from specimen charging and obtain a balance between electrical charging and resolution.

2.6 Atomic force microscopy (AFM) images were recorded on an Agilent 5420 microscope using a tapping-mode silicon probe (Budget Sensors SHR75, f_o = 75 kHz, k = 3 N/m) with a diamond-like carbon spike (radius ~1 nm, length ~100-200 nm). Scanning rate and resolution were set to 0.07 lines/s and 1024 x 1024, respectively.

2.7 Film thickness measurement was performed by surface wear technique with an AFM. An array of scratches were performed on the film in contact mode using a standard AFM silicon probe (NanoWorld Arrow FMR, f_o = 75 kHz, k = 2.8 N/m). Following, the scratches were imaged in tapping mode at 90° to avoid the scratched debris.

2.8 Annealing of films was carried out using a 2" quartz tube mounted on a single-zone split tube furnace (MTI OTF-1200) and connected to a vacuum pump, a mass flow controller, and a tank containing reducing gas (2.5 % H_2 and 97.5 % Ar). The quartz tube was evacuated to <50 mTorr after loading the nanodiamond

film-coated substrates and then brought back to atmospheric pressure with a 100 sccm flow of reducing gas for 30 min, before ramping the furnace to the desired temperature (200 °C, 300 °C, 400 °C) within 45 min. The annealing was carried out at the desired temperature for 4 h with reducing gas flowing at 20 sccm. The substrates were cooled to room temperature under continuous flow (~1 h) before examining them under the SEM and AFM.

2.9 Thermal conductivity measurements in the cross-plane direction of the thin films were performed using the 3ω method. Given that these films are comprised of nanoparticles arranged without perceivable ordering, it is expected that thermal conduction would be isotropic and that cross-plane thermal conductivity values are representative of all directions. Previously, the 3ω method has been used to measure the thermal conductivity of nano-diamond thin films produced by CVD by various groups [14-16]. This work utilizes the same experimental procedure, data reduction methodology, compensation for interfacial thermal resistances, validation against literature results, and uncertainty analysis outlined in our previous work on thermal transport in ultrananocrystalline diamond (UNCD) thin films [13], in which full details can be found. Briefly, a standard, straight four-probe line that functions as both a heater and thermometer of 50 μm width was patterned on the UNCD film using photolithography in accordance with the widely utilized 3ω heater/thermometer structure design [14-16]. The total length of the four-probe line was 1800 micrometers, while the length of the inner four-probe region was 900 micrometers. Following this, 10 nm chromium and 200 nm gold were deposited using electron beam evaporation and once the features obtained from photolithography are confirmed under an optical microscope, a lift-off process was performed which resulted in a 3ω line and four contact pads. This device was then placed in a 16-pin microchip commercial carrier and wire-bonding was used to make connections between the sample and chip carrier. The remaining experimental setup and data acquisition details follow those conventionally used for a 3ω measurement and are given in Ref. [13].

3. RESULTS AND DISCUSSION

3.1 Morphology of films as-deposited

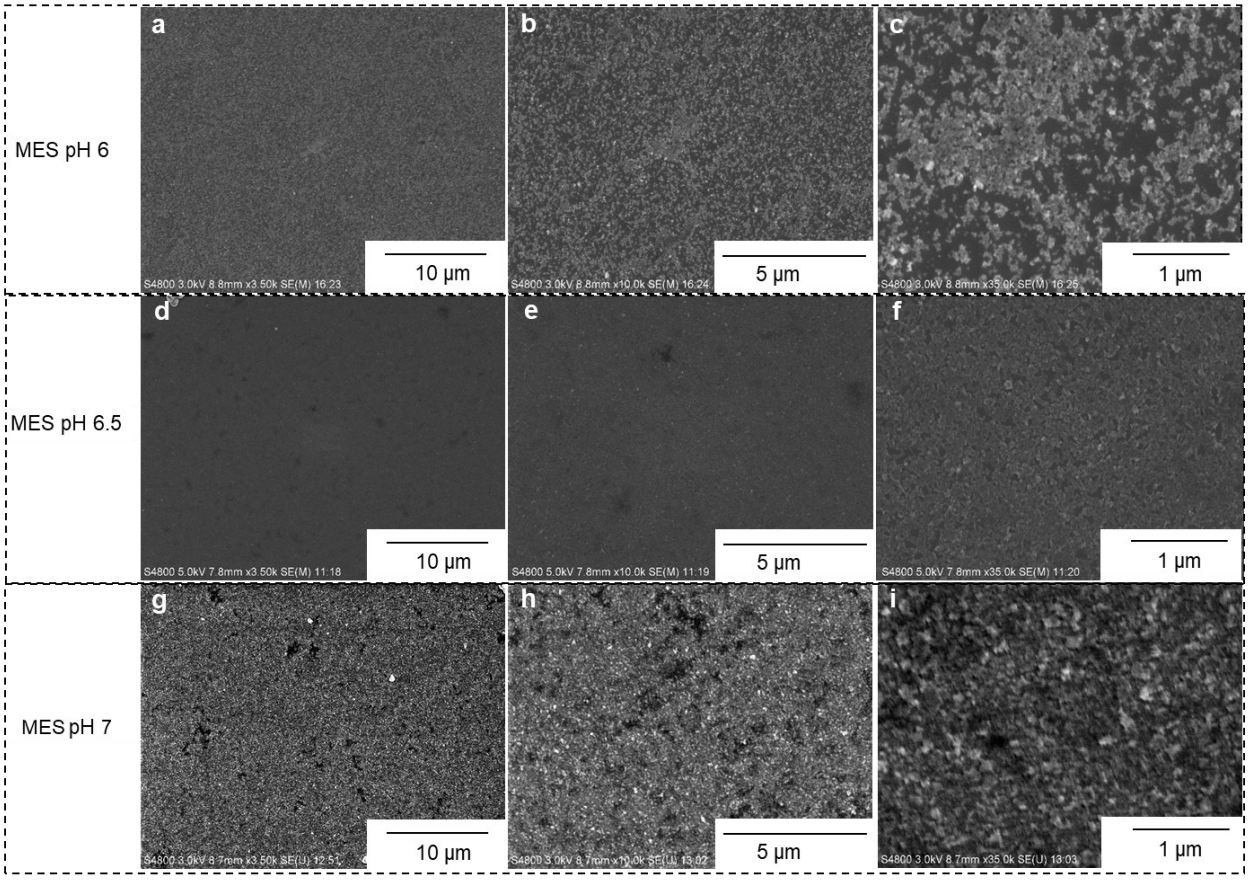

Figure 3. Film morphology observed using scanning electron microscopy at different magnifications when directed covalent assembly of ND-COOH was carried out 20 times in MES buffer of (a-c) pH 6, (d-f) pH 6.5, and (g-i) pH 7. Samples were not sputter coated to reduce charging. This allowed viewing the films unaltered.

The SEM images of as-deposited films shown in **Figure 3** and **Supporting Information Figure S1-3** were taken to investigate the film uniformity and surface coverage at the micron scale. After 20 deposition cycles in MES buffer pH 6, the films showed uniform surface coverage at 3.5k and 10k magnification, but incomplete surface coverage and non-uniform dispersion of nanodiamonds at 35k magnification. SEM images of the films deposited at pH 6.5 and pH 7 showed complete surface coverage at magnifications down to 35k. The films deposited at pH 6.5 showed lower surface roughness and thickness compared to the films deposited at pH 7. To compare these films to those from our prior work, we also prepared films using DI water-based sol using either bath sonication or horn sonication, as shown in **Supporting Information Figure S4**. The SEM images of nanodiamond films assembled using DI-water based sol prepared by horn sonication showed higher surface coverage and increased density compared to the films formed by bath sonication. However, the films assembled with MES buffer pH 7 (also horn sonicated) were much thicker than those obtained using DI water.

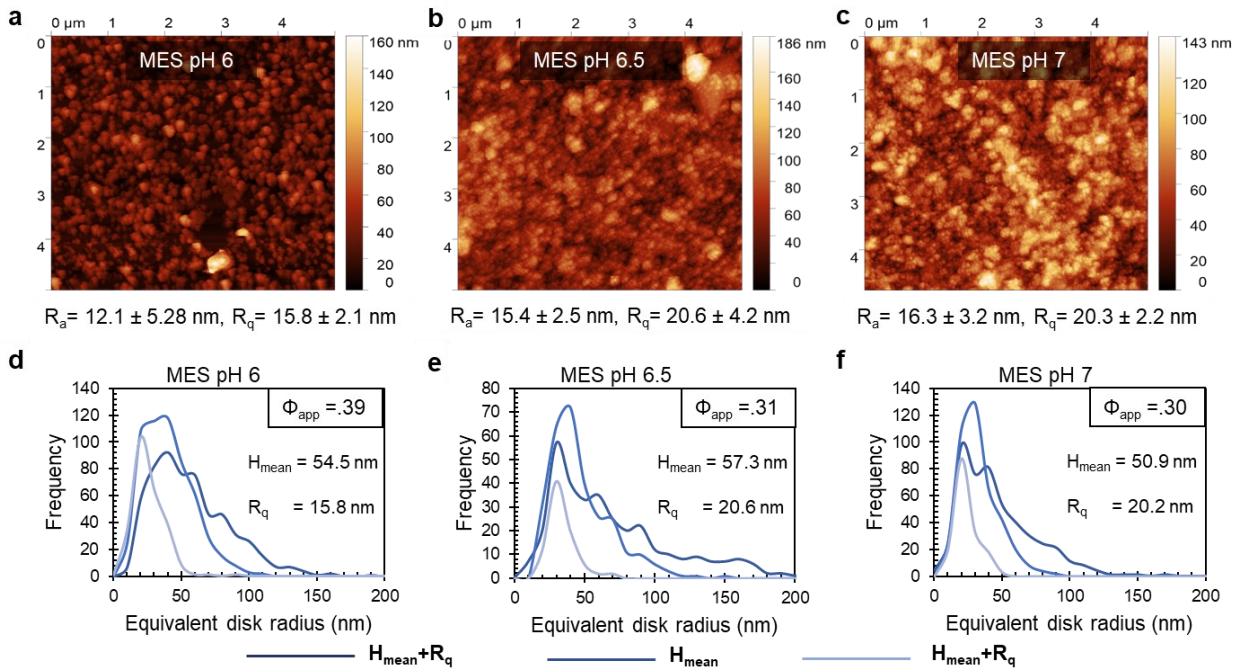

Figure 4. Film morphology observed using atomic force microscopy. (a-c) The topography of nanodiamond films obtained after 20 deposition cycles in MES buffer of pH 6, 6.5, and 7. The adjacent color scale indicates the relative height value. The root-mean-squared (RMS) surface roughness (R_q) values correspond to the average and standard deviation recorded on three chips. (d-f) The pore size distribution at different image sectioning height (mean height, mean height plus the RMS roughness, or mean height minus the RMS roughness), and the apparent porosity (Φ_{app}) as observed for the nanodiamond films deposited at pH 6, 6.5, and 7.

The AFM images obtained using a super-sharp probe were analyzed for quantifying surface roughness and film morphology (examples shown in **Figure 4a-c** and more furnished in **Supporting Information Figure S5**). The films deposited at pH 6.5 and pH 7 showed complete surface coverage and denser films compared to the films deposited at pH 6. The surface roughness of the films deposited at pH 7 was on the higher side compared to that of films deposited at pH 6.5. The comparison of film morphology was made using the apparent porosity (Φ_{app}) and the pore size distribution obtained by sectioning the AFM image at different heights.

The Φ_{app} was calculated as follows using high resolution (pixel size <5 nm) AFM images that were leveled by mean plane subtraction, aligned rows with the median method, corrected for horizontal scars, and had minimum data value shifted to zero.

$$\Phi_{app} = 1 - \frac{Total\ grain\ volume\ after\ rejecting\ spikes\ in\ the\ data}{Total\ volume\ of\ the\ image\ after\ rejecting\ spikes\ in\ the\ data} \quad (1)$$

To reject spikes in the data, image pixels exceeding mean height plus R.M.S. roughness (H_{mean} + R_q) were capped. The mean height after spike rejection ($H_{corrected\ mean}$) was then used to calculate apparent porosity as follows.

$$\Phi_{app} = 1 - \frac{H_{corrected\ mean}}{H_{mean}+Rq} \quad (2)$$

The Φ_{app} was found to be higher for films deposited at pH 6, whereas the Φ_{app} was similar for films deposited at pH 6.5 and 7. The pore-size distribution was obtained by watershed segmentation of AFM images that were cross-sectioned at either (H_{mean} + R_q), H_{mean}, or (H_{mean} – R_q). The area and perimeter values of the segmented pores were then used to generate the frequency distribution of the pore radius (=2*area/perimeter) as shown in **Figure 4d-f**. **Supporting Information Figure S6** shows that the images obtained with 5 nm resolution enabled analysis striking a balance between imaging resolution and imaging noise. At H_{mean} – R_q, the analysis represented the apparent deep pores. The average pore radius at H_{mean} – R_q for films deposited at pH 6, 6.5, and 7 were 31 ± 11, 39 ± 11 nm, and 29 ± 9 nm although their pore size distribution shows a peak at 20 nm, 20 nm, and 30 nm, respectively. This shows that the films deposited at pH 6.5 showed a slightly wider pore radius compared to the film deposited at pH 6 and 7. A similar observation was also made when cross-sectioning the AFM images at H_{mean}, and H_{mean} + R_q. The average pore radius at H_{mean} for films deposited at pH 6, 6.5, and 7 were 45 ± 20, 52 ± 22 nm, and 38 ± 15 nm, and their pore size distribution shows a peak at 20/40/60 nm, 40/70/90 nm, and 30/50 nm, respectively. Further, a small amount of left shift in pore size distribution for the pH 7 films when sectioning along H_{mean} + R_q, H_{mean}, and H_{mean} – R_q indicates that the pores have a higher aspect ratio.

3.2 Effect of annealing on film morphology

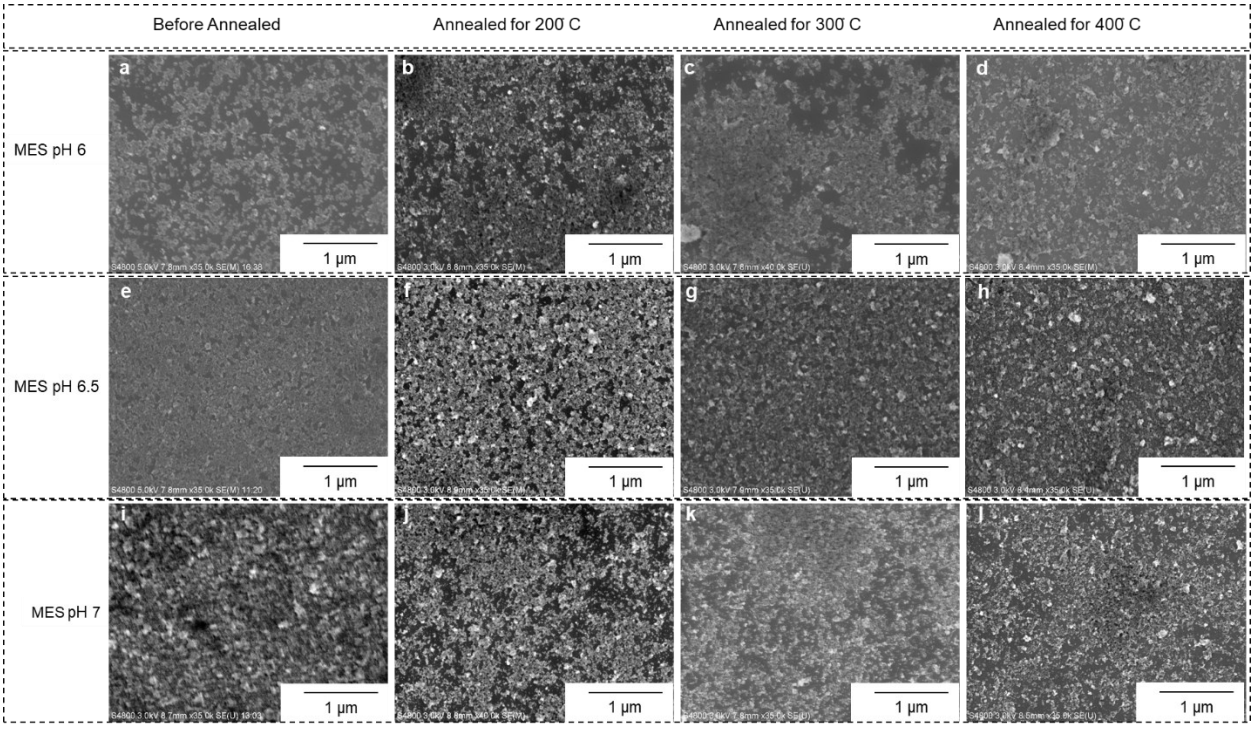

Figure 5. Effect of thermal annealing on the morphology of nanodiamond film as observed using SEM. The nanodiamond films were deposited at either pH 6 (a-d), 6.5 (e-h), or 7 (i-l), and annealed to either 200 °C (b, f, j), 300 °C (c, g, k), or 400 °C (d, h, l) for 4 h in 2.5 % H_2/ 97.5 % Ar. The scale bar in each image represents 1 µm.

The nanodiamond films assembled in MES buffer of pH 6, 6.5, and 7 were annealed sequentially at 200, 300, and 400 °C for 4 h accompanied with SEM and AFM examination after each anneal. **Figure 5** and **Supporting Information Figure S7-8** compare the surface morphology of nanodiamond films before and after annealing. The films deposited at pH 6 showed the spreading of nanodiamonds and an increase in surface coverage upon annealing 200 °C, but annealing at 300 °C showed signs of nanodiamond agglomeration. Noticeable agglomeration was seen in films deposited at pH 6.5 only after annealing at 400 °C, while the pH 7 samples showed agglomeration after annealing at 300 °C. Overall, the films deposited at either pH showed a noticeable agglomeration of the nanodiamonds when annealed at 400 °C, leading to a reduction in film uniformity and surface coverage. We hypothesize that the amides bonds were severed at temperatures exceeding 200 °C similar to that observed in microporous organic polymers,[17] followed by their self-assembly into larger nanodiamond agglomerates.[18]

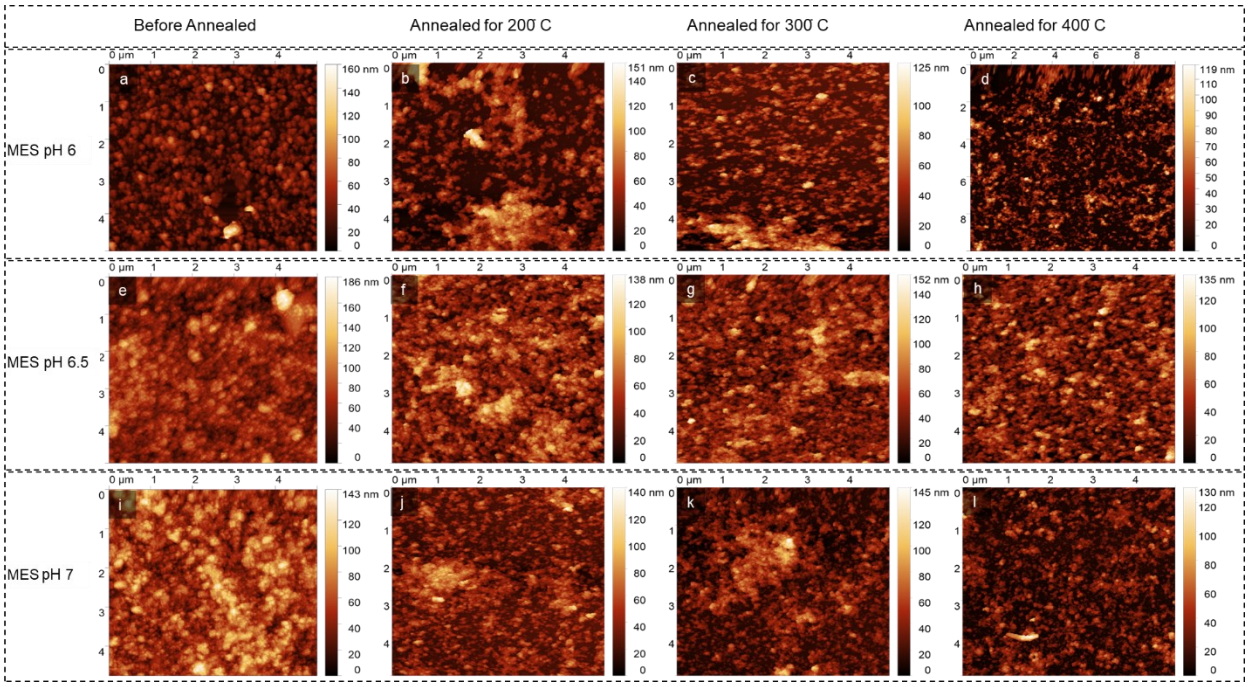

Figure 6. Effect of thermal annealing on the morphology of nanodiamond films as observed using 5 µm x 5 µm AFM images (1024 x 1024). The films were deposited at either pH 6 (a-d), 6.5 (e-h), or 7 (i-l), and annealed to either 200 °C (b, f, j), 300 °C (c, g, k), or 400 °C (d, h, l) for 4 h in 2.5 % H_2/ 97.5 % Ar.

Like the SEM results, AFM images in **Figure 6** and **Supporting Information Figures S9-10** confirm a change in surface morphology and aggregation upon annealing. **Supporting Figure 11** shows the pore size distribution and Φ_{app} obtained after annealing the films assembled at pH 6, 6.5, and 7. The Φ_{app} was seen to increase as a result of annealing for either film, especially annealing at 400 °C led to the highest Φ_{app} of 0.51, 0.38, and 0.46 for films assembled at pH 6, 6.5, and 7, respectively. For all the nanodiamond films, as the nanodiamonds aggregated with annealing, more of the substrate were revealed and the H_{mean} was

found to decrease in areas imaged for pore analysis. The average pore radius at H_{mean} after annealing the pH 6, 6.5, and 7 films at 400 °C (4 h) were 58.9±28.4 nm, 37.7±9.8 nm, and 41.1±19 nm, respectively, while 66.3±29.5nm, 48.2±15 nm, and 53.9±19.9 nm were recorded was at $H_{mean+Rq}$, and 34.9±11 nm, 33.9±7.5 nm and 28.8±7.4 nm at $H_{mean-Rq,}$ respectively. This showed that pores remained conical in shaped despite the nanodiamond aggregation on thermal annealing.

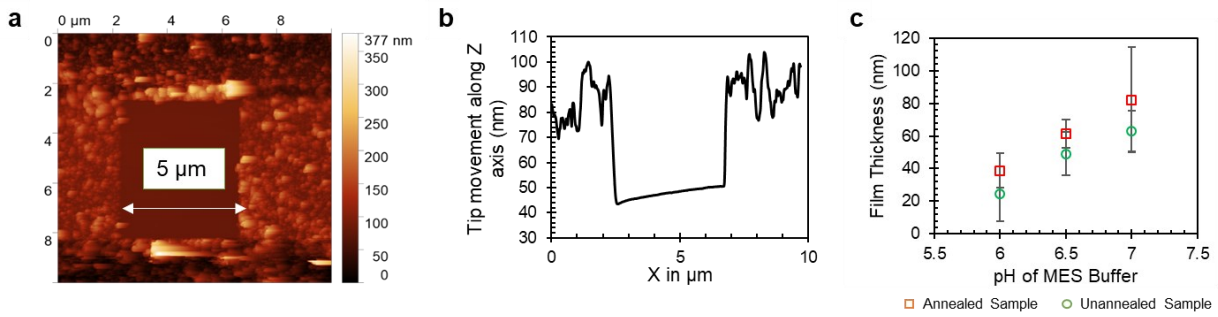

Figure 7. (a) An example 5 µm x 5 µm square scratched in the nanodiamond film. (b) An example cross-section profile was obtained from the square. (c) The average film thickness obtained for the nanodiamond films deposited with MES buffer of pH 6, 6.5, and 7 before annealing and after annealing at 400 °C. The error bar indicates the average surface roughness of the films. The film thickness was calculated as the average height of the points on either side of the square minus the average height of the points inside the square.

To perform the film thickness measurement, the scanner was fixed in a position and a tapping mode 10 µm x 10 µm image was taken, followed by scratching (10 times) a 5 µm x 5 µm area within the imaged area, causing the removal of the nanodiamond film as shown in **Figure 7a-b**. The film thickness was measured by leveling the data by fitting a plane in the scratched portion, shifting the minimum value to zero, and measuring the averaged difference in the height value for the area inside and outside the scratched area. Thus, obtained film thickness values over three distinct areas (**Figure 7c**) show increasing film thickness with the pH of MES buffer. The as-deposited samples showed an average film thickness of 24 ± 16.6 nm. 49.1 ± 13.3 nm and 63 ± 12.5 nm for pH 6, 6.5, and 7, respectively. The corresponding average film thickness after annealing was found to be higher but statistically indifferent; pH 6, pH 6.5, and pH 7 samples showed 38.8 ± 10.4 nm, 61.5 ± 8.7 nm, and 81.9 ± 32.2 nm film thickness, respectively. The observed higher average film thickness is believed to occur as a result of increasing aggregation and porosity of the film.

3.3 Thermal Characterization

Figure 8 shows the temperature-dependent thermal conductivity values obtained from the 3ω method for nanodiamond films, with porosity and the thermal resistances at the heater-film and film-substrate interfaces compensated for as detailed in Ref. [13]. For unannealed samples, as shown in **Figure 8a**, the

thermal conductivity of the films deposited at pH 6 and pH 6.5 showed an increase with temperature, similar to that observed previously [13] above 300 K for very thin nanodiamond films with significant variations in film thickness. This trend, along with the sizable increase in thermal conductivity near 340 K for the pH 6 sample, may be related to improved interparticle phonon transmission occurring as stage temperature was increased. The pH 7 sample showed the largest thermal conductivity value measured at 310 K, and subsequent measurements at higher temperatures resulted in temperature differences across the thin film sample that were too small to be reliably used in determining thermal conductivity and were thus omitted. The pH 7 sample's thermal conductivity was found to be comparable to the upper range of values previously reported for similarly assembled nanodiamond films [13].

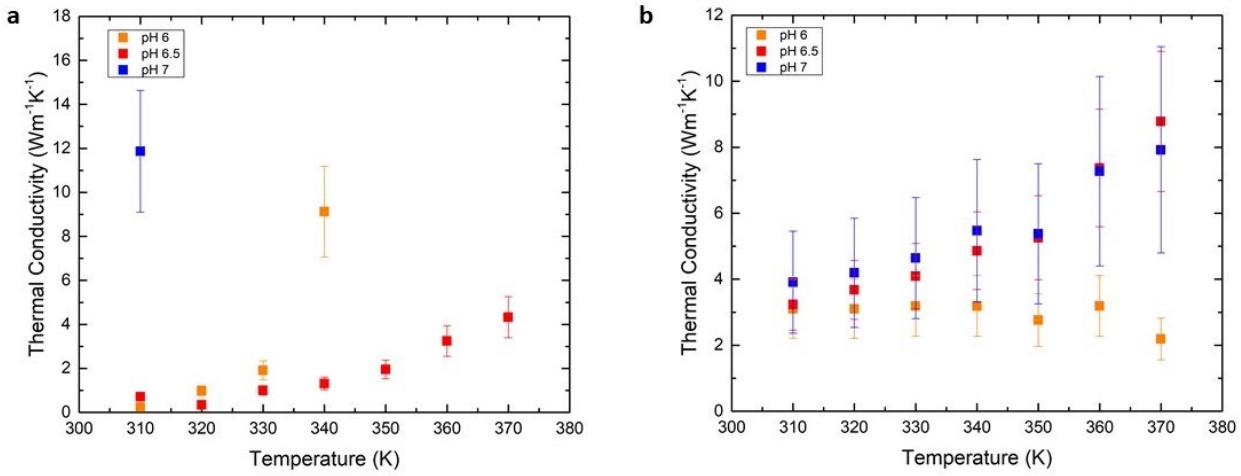

Figure 8. Thermal conductivity of UNCD thin films realized through different pH for (a) unannealed and (b) annealed samples.

The same thermal conductivity measurements were performed for thin films created at varying pH values with annealing at 400 °C as described above, with results given in **Figure 8b**. The thermal conductivity values of all the annealed samples were comparable near room temperature regardless of deposition pH. However, the observed temperature-dependence deviates for the pH 6 sample compared to pH 6.5 and pH 7. Both types of trends were observed in our previous measurements on UNCD thin films [13]. The pH 6 sample demonstrated a slight decrease in thermal conductivity with increasing temperature but within experimental uncertainty. In contrast, the pH 6.5 and pH 7 samples exhibited a general increase in thermal conductivity with increasing temperature, though this trend is likewise comparable to the span of the point-to-point uncertainty level such that this cannot be said with certainty.

From the structural characterization performed on annealed samples, it was shown that annealing does induce film morphology changes, specifically an increase in aggregation and porosity compared to the unannealed films. Here, we observe an improvement in thermal conductivity near room temperature for the pH 6 and 6.5 samples, and a decrease for the pH 7 sample compared to the unannealed cases, respectively. This suggests that the morphology changes associated with annealing may have a complex relationship with thermal conductivity. Specifically, substantial changes in aggregation can lead to

significant void space or uneven films (negative effect), or else improve interparticle phonon transmission (positive effect). The net result in terms of thermal conductivity magnitude would depend then on the relative magnitude of these effects and the efficacy of interparticle phonon transmission within the film before annealing. Overall, for the annealed samples the thermal conductivity values approach those previously reported of the thinnest samples, i.e. 10 cycle films, tested in [13] where the value of thermal conductivity for thinnest film lies in the range 2.5 W m^{-1} K^{-1} – 10 W m^{-1} K^{-1}.

To quantify and compare inter-particle phonon transmission within the measured thin films, the thermal conductivity data was analyzed using the phonon hopping model originally developed by Braginsky *et al.* [18] and previously utilized by Shamsa *et al.* [14] for nanocrystalline diamond films. The model assumes that the phonon hopping follows bulk-like scattering rules within each particle but the phonon hopping from one grain to another is governed by a semi-empirical boundary transparency parameter *t*. This parameter simply describes the probability that a phonon will hop to a neighboring particle, with a larger value of *t* indicating a greater degree of phonon movement across boundaries. The model's prediction for the thin film thermal conductivity κ is calculated using:

$$\kappa = k_B T \int_0^{\frac{\theta_D}{T}} \frac{\kappa_i F(x) t \tilde{S} \phi}{\hbar {k_B}^{-1} \kappa_i a^2 d + k_B \theta_D F(x) t \tilde{S} \phi} dx \tag{3}$$

where,

$$F(x) = \frac{9}{2}\left(\frac{T}{\theta_D}\right)^4 \frac{x^4 e^x}{(e^x-1)^2}\left(x - \frac{\theta_D}{T}\right)^2 \quad . \tag{4}$$

Here, θ_D is the Debye temperature, *a* is the lattice constant and *d* is the average particle size, $\tilde{S}(= d^2)$ is the mean area of the interparticle boundary, $\hbar$ is the Planck constant, k_B is the Boltzmann's constant, ϕ is the size fluctuation factor, and κ_i is the intrinsic bulk-like thermal conductivity associated with the inner portions of each particle. Here, we utilize the following values for the nanodiamond thin films based on either literature values as indicated or experimentally determined morphology: $\phi = 0.87$ [19], θ_D = 1860 K [20], κ_i= 2200 W m^{-1} K^{-1} [21, 22], *a* = 0.357 nm [23], and *d* = 30 nm for the average aggregate diameter as discussed above. The experimentally measured thermal conductivity values for each film were then used to extract values of the boundary transparency parameter *t* for each sample. The boundary transparency parameter values for both unannealed and annealed samples are plotted in **Figure 9**.

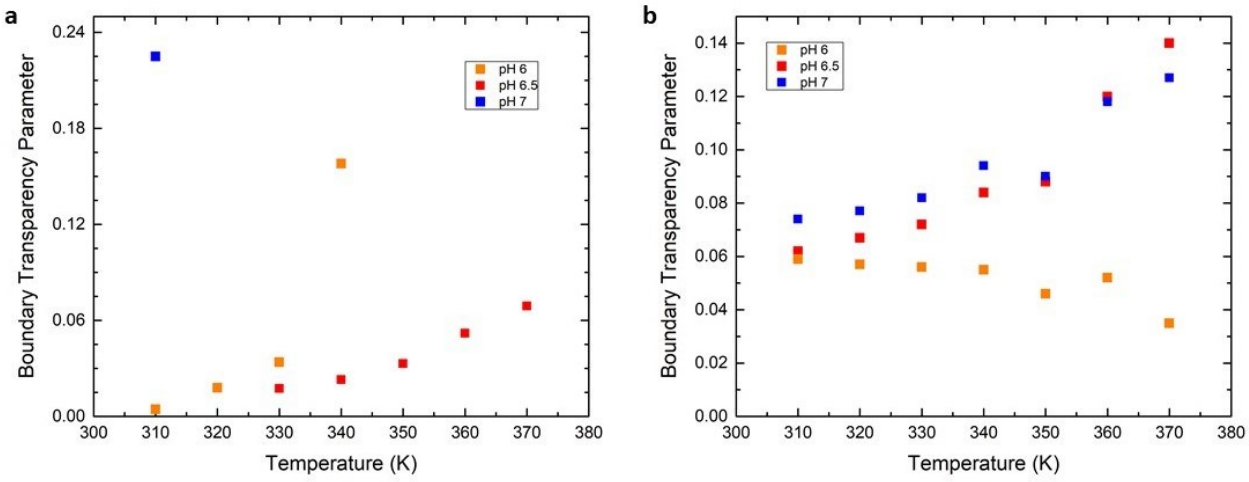

Figure 9. Extracted boundary transparency parameters for (a) unannealed and (b) annealed nanodiamond film samples.

In **Figure 9a** it can be seen that the boundary parameter *t* generally scales with thermal conductivity as expected, with the high thermal conductivity for pH 7 being facilitated by a higher degree of phonon transport across interparticle boundaries and a relatively wide span of values for *t* across samples. When this same model is applied to the annealed data (**Figure 9b**), the boundary parameter shows much less variation across samples, again similar to the thermal conductivity. This would seem to suggest that annealing works to homogenize interfaces within the films and reduce sample-to-sample variation. This homogenization may come at the expense of potentially less efficient phonon transmission across interfaces as seen for the pH 7 sample. Further work with a greater number of samples would be needed to conclusively determine if these hypotheses are correct. However, if confirmed this could make diamond nanoparticle thin films a convenient material system through which to study fundamental phonon-interface dynamics. In addition, this would further strengthen the need to tightly control interfacial quality in nanoparticle-based materials.

Here demonstrated nanodiamond films with improved thermal conductivity hold potential for cooling silicon and non-silicon electronic devices as effective heat spreading dielectrics and reducing overall power consumption. Thermal management is further a big issue in flexible electronics where the flexible polymeric substrates have thermal conductivity less than 1 W/m-K. The nanodiamond films demonstrated here have > 1 W/m-K and can be deposited on flexible substrates where the conventional chemical vapor deposition methods have failed due to substrate incompatability. Thus, the nanodiamond films hold potential as thermally conducting dielectric coatings in flexible electronics to provide effective thermal management, which further has implications in improving user comfort in wearable devices. The tuning of the film morphology (e.g. porosity) holds potential to aid bio-integration, integration of electronics with biological tissues for implanted electronics.

4. CONCLUSIONS

In summary, we have examined the effect of using 10 mM MES buffer as a placement for deionized water or 10 mM KCl in the directed covalent assembly of detonation nanodiamonds. It was shown that the buffer pH can be varied to tune the surface coverage, film thickness, film apparent porosity, pore size distribution, and thermal conductivity. As seen via SEM and AFM, a pH 6.5 or pH 7 buffer leads to a continuous surface coverage and a similar apparent porosity (~30%), while a pH 6 buffer leads to discontinuous films and more porous films (~65%). Further, the films deposited at pH 7 showed smaller pore sizes and a higher thermal conductivity in comparison to films deposited at pH 6.5. The as-deposited films at pH 7 showed a thermal conductivity as high as 12 ± 2.5 W m^{-1} K^{-1} at 310 K, which is comparable to that obtained for UNCD films obtained via chemical vapor deposition. However, sequential thermal annealing of the nanodiamond films at temperatures up to 400 °C led to the aggregation of nanodiamond to segregated islands, loss of surface coverage, and increase in porosity. The thermal conductivity of all the annealed samples was comparable near room temperature regardless of deposition pH. The pH 6.5 and pH 7 samples exhibited a general increase in thermal conductivity with increasing temperature, while pH 6 samples exhibited statistically similar thermal conductivity with increasing temperature. The use of a phonon hopping model to deduce the phonon transfer at the grain-grain boundary indicates that annealing works to homogenize interfaces within the films and reduce sample-to-sample variation but it comes at the expense of less efficient phonon transmission across interfaces. Overall, the results demonstrate a way to achieving porous, low-cost nanocrystalline diamond thin films with tunable film morphology and thermal conductivity for electronics and biomedical applications.

Supporting Information

Supporting Information provides Figures S1-11 referenced in the main text.

Acknowledgements

The research reported in this publication was supported by the National Science Foundation under Grant No. 1636289. We are thankful to the staff members at the Institute for Micromanufacturing and the Center for Biomedical Engineering and Rehabilitation Sciences. N. H. Patoary, and T. Desai contributed equally to leading this work.

Reference

[1] M. Shabani, C. Abreu, J. Gomes, R. Silva, F. Oliveira, Effect of relative humidity and temperature on the tribology of multilayer micro/nanocrystalline CVD diamond coatings. Diamond and Related Materials, 73 (2017) 190-198.

[2] A.V. Sumant, D.S. Grierson, J.E. Gerbi, J. Birrell, U.D. Lanke, O. Auciello, J.A. Carlisle, R.W. Carpick, Toward the Ultimate Tribological Interface: Surface Chemistry and Nanotribology of Ultrananocrystalline Diamond. Advanced materials, 17 (2005) 1039-1045.
[3] A. Grill, Tribology of Diamondlike Carbon and Related Materials: an Updated Review. Surface and Coatings Technology, 94–95 (1997) 507-513.
[4] A. Krauss, O. Auciello, D. Gruen, A. Jayatissa, A. Sumant, J. Tucek, D. Mancini, N. Moldovan, A. Erdemir, D. Ersoy, Ultrananocrystalline diamond thin films for MEMS and moving mechanical assembly devices. Diamond and Related Materials, 10 (2001) 1952-1961.
[5] X.-R. Lu, M.-H. Ding, C. Zhang, W.-Z. Tang, Comparative study on stability of boron doped diamond coated titanium and niobium electrodes. Diamond and Related Materials, 93 (2019) 26-33.
[6] W. Zhang, A.D. Radadia, Towards a Boron-Doped Ultrananocrystalline Diamond Electrode-Based Dielectrophoretic Preconcentrator. Analytical chemistry, 88 (2016) 2605-2613.
[7] D. Damm, A. Contin, L. Cardoso, V. Trava-Airoldi, D. Barquete, E. Corat, A novel method to mitigate residual stress in CVD diamond film on steel substrates with a single intermediate layer. Surface and Coatings Technology, 357 (2019) 93-102.
[8] K.-H. Yang, R.J. Narayan, Biocompatibility and functionalization of diamond for neural applications. Current Opinion in Biomedical Engineering, 10 (2019) 60-68.
[9] B. Shi, Q. Jin, L. Chen, O. Auciello, Fundamentals of ultrananocrystalline diamond (UNCD) thin films as biomaterials for developmental biology: Embryonic fibroblasts growth on the surface of (UNCD) films. Diamond and Related Materials, 18 (2009) 596-600.
[10] C.E. Nebel, D. Shin, B. Rezek, N. Tokuda, H. Uetsuka, H. Watanabe, Diamond and biology. Journal of the Royal Society Interface, 4 (2007) 439-461.
[11] Y. Muranaka, H. Yamashita, H. Miyadera, Low temperature (∼ 400° C) growth of polycrystalline diamond films in the microwave plasma of CO/H2 and CO/H2/Ar systems. Journal of Vacuum Science & Technology A: Vacuum, Surfaces, and Films, 9 (1991) 76-84.
[12] X. Xiao, J. Birrell, J. Gerbi, O. Auciello, J. Carlisle, Low temperature growth of ultrananocrystalline diamond. Journal of Applied Physics, 96 (2004) 2232-2239.
[13] N.H. Patoary, A. Rai, K.P. Patel, A. Rebecca, W. Zhang, A.J. Ulrich, M. Galib, T. Desai, S. Zivanovic, M. Yousufuddin, A.L. Moore, A.D. Radadia, Directed covalent assembly of nanodiamonds into thin films. Diamond and Related Materials, 101 (2020) 107605.
[14] M.A. Angadi, T. Watanabe, A. Bodapati, X. Xiao, O. Auciello, J.A. Carlisle, J.A. Eastman, P. Keblinski, P.K. Schelling, S.R. Phillpot, Thermal transport and grain boundary conductance in ultrananocrystalline diamond thin films. Journal of Applied Physics, 99 (2006) 114301.
[15] M. Shamsa, S. Ghosh, I. Calizo, V. Ralchenko, A. Popovich, A. Balandin, Thermal conductivity of nitrogenated ultrananocrystalline diamond films on silicon. Journal of Applied Physics, 103 (2008) 083538.
[16] M. Mohr, L. Daccache, S. Horvat, K. Bruhne, T. Jacob, H.-J. Fecht, Influence of grain boundaries on elasticity and thermal conductivity of nanocrystalline diamond films. Acta Materiala, 122 (2017) 92-98.
[17] V.M. Suresh, S. Bonakala, H.S. Atreya, S. Balasubramanian, T.K. Maji, Amide functionalized microporous organic polymer (Am-MOP) for selective CO2 sorption and catalysis. ACS applied materials, 6 (2014) 4630-4637.
[18] A.S. Barnard, Self-assembly in nanodiamond agglutinates. Journal of Materials Chemistry, 18 (2008) 4038-4041.
[19] L. Braginsky, N. Lukzen, V. Shklover, H. Hofmann, High-temperature phonon thermal conductivity of nanostructures. Physical Review B, 66 (2002) 134203.
[20] N.W. Ashcroft, N.D. Mermin, in, New York: Holt, Rinehart and Winston, 1976.
[21] J. Olson, R. Pohl, J. Vandersande, A. Zoltan, T. Anthony, W. Banholzer, Thermal conductivity of diamond between 170 and 1200 K and the isotope effect. Physical Review B, 47 (1993) 14850.

[22] L. Wei, P. Kuo, R. Thomas, T. Anthony, W. Banholzer, Thermal conductivity of isotopically modified single crystal diamond. Physical review letters, 70 (1993) 3764.
[23] G.S. Gildenblat, P. Schmidt, DIAMOND (C), in: Handbook Series on Semiconductor Parameters: Volume 1: Si, Ge, C (Diamond), GaAs, GaP, GaSb, InAs, InP, InSb, World Scientific, 1996, pp. 58-76.